RSC Advances

PAPER

Cite this: *RSC Adv.*, 2020, **10**, 23615

Raman scattering and red emission of Mn^{4+} in $La_{0.7}Sr_{0.25}Na_{0.05}Mn_{0.7}Ti_{0.3}O_3$ manganite phosphor for LED applications

Z. Raddaoui,[a] S. El Kossi,[a] B. Smiri,[b] Thamraa Al-shahrani,[c] J. Dhahri[a] and H. Belmabrouk*[d]

Received 5th May 2020
Accepted 4th June 2020

DOI: 10.1039/d0ra04033a

rsc.li/rsc-advances

The vibrational and optical properties of an $La_{0.7}Sr_{0.25}Na_{0.05}Mn_{0.7}Ti_{0.3}O_3$ (LSNMT) polycrystalline sample produced *via* a solid-state reaction were studied. The Raman spectrum at room temperature reveals the chemical disorder in our compound. The optical gap and Urbach energy were estimated on the basis of the absorption spectrum. Moreover, the polycrystalline manganite radiates in the near-infrared light (1000 nm) with 514.5 nm light excitation and in the temperature range from 10 K to 300 K. Crystal field analysis suggests that only the Mn^{4+} luminescent center is found in LSNMT. The measured activation proves that our compound possesses good thermostability. The chromaticity coordinates prove that the emission of the LSNMT sample occurs in the near-infrared region. All analytical findings demonstrate that LSNMT manganite has substantial prospective applications in white luminescent devices.

1. Introduction

Due to the warning from numerous research committees on pollution issues against the global industrial development, a clean nanotechnology system including multifunctional nanoparticles has become important owing to their potential applications in several research fields with actual and more efficient impacts in several areas of research.[1–3]

More precisely, manganite-based perovskite-type oxides of the composition $A_{1-x}B_xMnO_3$ have appeared to be an attractive class of performing materials because of their low cost and abundance on the earth.[4,5] Their diversity and promising physical properties deserve significant interest in numerous nanotechnology-related applications such as optoelectronic devices, electrocatalysis, and memory storage devices. For these reasons, worldwide research activity is devoted to understanding the origin of these potential characters.[6,7]

However, the functionality of manganite is well known for its magnetic properties and particularly colossal magnetoresistive behavior. These features represent the most important discovery and revolution of the magnetic system. It is accompanied by the magnetic transition, which is explained by the double exchange and superexchange phenomena.[8] Usually, magneto-transport characteristics have been connected to the double exchange phenomena, which are governed by the movement of the e_g electrons from Mn^{3+} to Mn^{4+}.[9] These proprieties have attracted considerable attention and bring a new theory and model to explain the interactions between transport and magnetic behaviors such as spin-glass and charge ordering.[10]

The simplicity of structure has been extensively exploited as a clue for numerous applications due to the moderation of properties by the substitution of A and/or B, resulting in a variety of structures that could play a key role to manipulate capacity and performance.[11] The occupation of the transition metal B in the octahedral system produced a splitting of the d orbital into two degenerated e_g orbitals and three t_{2g} orbitals. This step was pursued following the effect of Jahn–Teller to create a stable structure with two energies states (σ^*, σ) in e_g orbital occupation and the covalent oxygen-related intermediate species.[12] In fact, the variation of the ionic radii is a type of chemical pressure that creates a deformation in BO_6 from the perfect ceramic, which causes large degrees of strain and distorts the surrounding lattice and yields a variety of unit cells and lattice parameters.[13] Full knowledge of these factors is important to underline the high impact of microstructural properties on the double exchange phenomena that is the source of the physics of the properties in perovskites. This strongly relies on the B–O bond length (d_{B-O}) and the (θ_{B-O-B}) bond angle.[14]

Strontium-substituted lanthanum manganite ($La_{0.7}Sr_{0.3}MnO_3$) as a typical magnetic material opens the door to numerous investigations on the origin of its colossal

[a]*Laboratoire de la Matière Condensée et des Nanosciences, Université de Monastir, Faculté des Sciences de Monastir, Avenue de l'environnement, 5019 Monastir, Tunisia*
[b]*Laboratoire de Micro-optoélectroniques et Nanostructures, Université de Monastir, Faculté des Sciences Monastir, Avenue de l'environnement, 5019 Monastir, Tunisia*
[c]*Department of Physics, College of Science, Princess Nourah Bint Abdulrahman University, Riyadh, Saudi Arabia*
[d]*Department of Physics, College of Science at Zulfi, Majmaah University, Zulfi 11932, Saudi Arabia. E-mail: Ha.Belmabrouk@mu.edu.sa*

magnetoresistive properties. These properties are explained in terms of the interaction between the structural distortion and magnetic mechanisms related to the magnetic coupling between Mn^{4+} and Mn^{3+}. Abdelmoula *et al.*[15] reported that the substitution by a monovalent element can improve the physical properties of manganite. In fact, they investigated the impact of Na incorporation in $La_{0.7}Sr_{0.3}MnO_3$, which proves that the doped manganite oxides ($La_{0.7}Sr_{3-x}Na_xMnO_3$) constitute very attractive candidates as potential giant magneto-resistance compounds. Similarly, Kossi *et al.*[16] have reported that $La_{0.7}Sr_{0.025}Na_{0.05}MnO_3$ and $La_{0.7}Sr_{0.025}Ka_{0.05}MnO_3$ show a giant magnetocaloric property and announced giant dielectric properties with the partial substitution of Mn by Ti. In the same way, more recent studies proved that $La_{0.7}Sr_{0.3}MnO_3$ and its derivatives can be the next-generation energy technologies for clean power generation due to their multiferroic properties and their hopeful applications in numerous domains.[17]

Moreover, recent progress reveals that manganites present alternative materials to phosphorus as a luminescent matrix and open up new fields of investigation.[18] However, much work remains to be done to achieve high luminescence performance adaptable to large-scale technological applications. In fact, manganite is influenced by the doping ion, *i.e.*, manganese ion (Mn^{4+}). This tetravalent ion is luminescent. It is able to emit red light when it is excited by blue or near-UV light.[19] In addition, the luminescence characteristics can be tailored and enhanced by varying the dopant concentration, grain size, synthesis process, and temperature of sintering. However, the most important factor influencing these characteristics is the choice of the dopant and the doping site that directly affect the characteristic of MnO_6 octahedrons.[20]

In this study, LSNMT polycrystalline manganite was prepared *via* a classical solid-state method that requires high temperatures. The vibrational properties of the LSNMT manganite were studied *via* Raman spectroscopy. The luminescence characteristics of our manganite compound were investigated from its absorption spectrum and photoluminescence (PL) spectrum. The thermal stability of LSNMT was deduced from its PL spectra, which depends on the temperature value.

2. Background

Raman spectroscopy is a well-known technique that provides the chemical and structural knowledge of diverse compounds using the data of the vibrational states of a matter. Raman-shifted photons have either Stokes scattering or anti-Stokes scattering. Since phonons are bosons, the Stokes and anti-Stokes intensities are respectively related to $(n + 1)$ or n. The quantity n denotes the occupation number. Since the Stokes intensity is more intense than the anti-Stokes intensity, only the Stokes intensity is usually registered and interpreted in traditional Raman spectroscopy.[21]

In general, to compute the intensity of the compounds during Raman scattering some equations are required. We recall hereafter some of these equations. Let $\hbar$ be the reduced Planck constant, ω_i denotes the angular frequency of the incident photon, ω_s is the angular frequency of the scattered photon, ω_p is the angular frequency of the scattered phonon, k_B is the Boltzmann constant and T is the absolute temperature.

It is well known that the Stokes process corresponds to the emission of a phonon, whereas the anti-Stokes process corresponds to the absorption of a phonon. We deduce that the energy change during these phenomena is given by:

$$\begin{cases} \hbar\omega_s = \hbar\omega_i - \hbar\omega_p & \text{for Stokes process} \\ \hbar\omega_s = \hbar\omega_i + \hbar\omega_p & \text{for anti-Stokes process} \end{cases} \quad (1)$$

The intensities I_S and I_{AS} of the first-order scattering by a phonon or more generally by a boson are given by:

$$\begin{cases} I_S \propto I_i\chi''(\omega){\omega_s}^3[n(\omega, T) + 1] & \text{for Stokes process} \\ I_{AS} \propto I_i\chi''(\omega){\omega_s}^3 n(\omega, T) & \text{for anti-Stokes process} \end{cases} \quad (2)$$

where $\chi''(\omega)$ is the line shape response of a harmonic mode.

The occupation number $n(\omega,T)$ of phonons at thermal equilibrium is given by:

$$n(\omega, T) = \frac{1}{\exp\left(\frac{\hbar\omega}{k_B T}\right) - 1} \quad (3)$$

The ratio of the intensities related to the second-order scattering is approximated by the following equation:

$$\left(\frac{I_S}{I_{AS}}\right)^2 \approx \left(\frac{n(\omega, T) + 1}{n(\omega, T)}\right)^2 \quad (4)$$

Optical characteristics are one of the most interesting parameters to estimate the light efficiency. One of them, the optical band gap (E_g) can be obtained by employing the basic absorption.

They are determined using the following formula:[22]

$$\alpha h\nu = B(h\nu - E_g)^n \quad (5)$$

A crystallized ceramic is ideally perfect. The absence of this condition is attributed to a defect in the solid, which can be connected to a defect caused by impurities and distortion.

The Urbach energy E_u describes the disorder of a sample.

From the change in the absorption coefficient, it is possible to extract the disorder in the sample, resulting from this equation.

$$\alpha = 2.303 \times (A/d) \quad (6)$$

$$\alpha = \alpha_0 \exp\left(\frac{h\nu}{E_u}\right) \quad (7)$$

where d is the thickness and A is the optical absorbance of the sample.

3. Experimental procedure

The LSNMT sample was produced by the well-known solid-state method. The metal precursors La_2O_3, $SrCO_3$, Na_2O_3, MnO_2 and TiO_2 were of high purity (99%). The polycrystalline manganite

preparation has been discussed in our previous work.[16] Furthermore, Fig. 1 depicts the steps of the process of synthesis.

The X-ray structure analysis by the Rietveld refinement was discussed in our previous work.[16] It was noted that LSNMT crystallizes in the rhombohedral $R\bar{3}c$ structure without any detectable secondary phase, with lattice parameters $a = b = 5.536(3)$ Å, $c = 13.438(3)$ Å and cell volume $V = 356.75(2)$ Å^3. It is also important to recall the values of the bond length $d_{Mn-O-Mn} = 1.97(1)$ Å and the bond angle $\theta_{Mn-O} = 164.24(3)°$.

The Raman data were recorded in the frequency range 80 to 1000 cm^{-1} using a LABRAM HR800 Raman spectrometer. The spectral resolution of the system was 3 cm^{-1} with a power of about $P = 50$ mW and $\times 10$ objective (focus diameter larger than 10 microns). The scattered radiation was detected by a 1024 $\times$ 256 CCD camera. Our compound was excited by a 532 nm laser at room temperature.

The UV-Vis-NIR spectra at room temperature in the wavelength range of 150 to 1500 nm were measured on a Shimadzu UV-3101PC spectrophotometer with a source emitting wavelength radiations on a pellet of our compound.

The photoluminescence (PL) data were recorded between 10 K and 300 K while keeping the sample in a closed-cycle helium circulation cryostat. The sample was excited by employing a 514.5 nm line of the continuous wave Ar^+ laser and a situated power excitation of 50 W cm^{-2}. Spectral analysis of the luminescence measurements was dispersed using Jobin Yvon HRD1

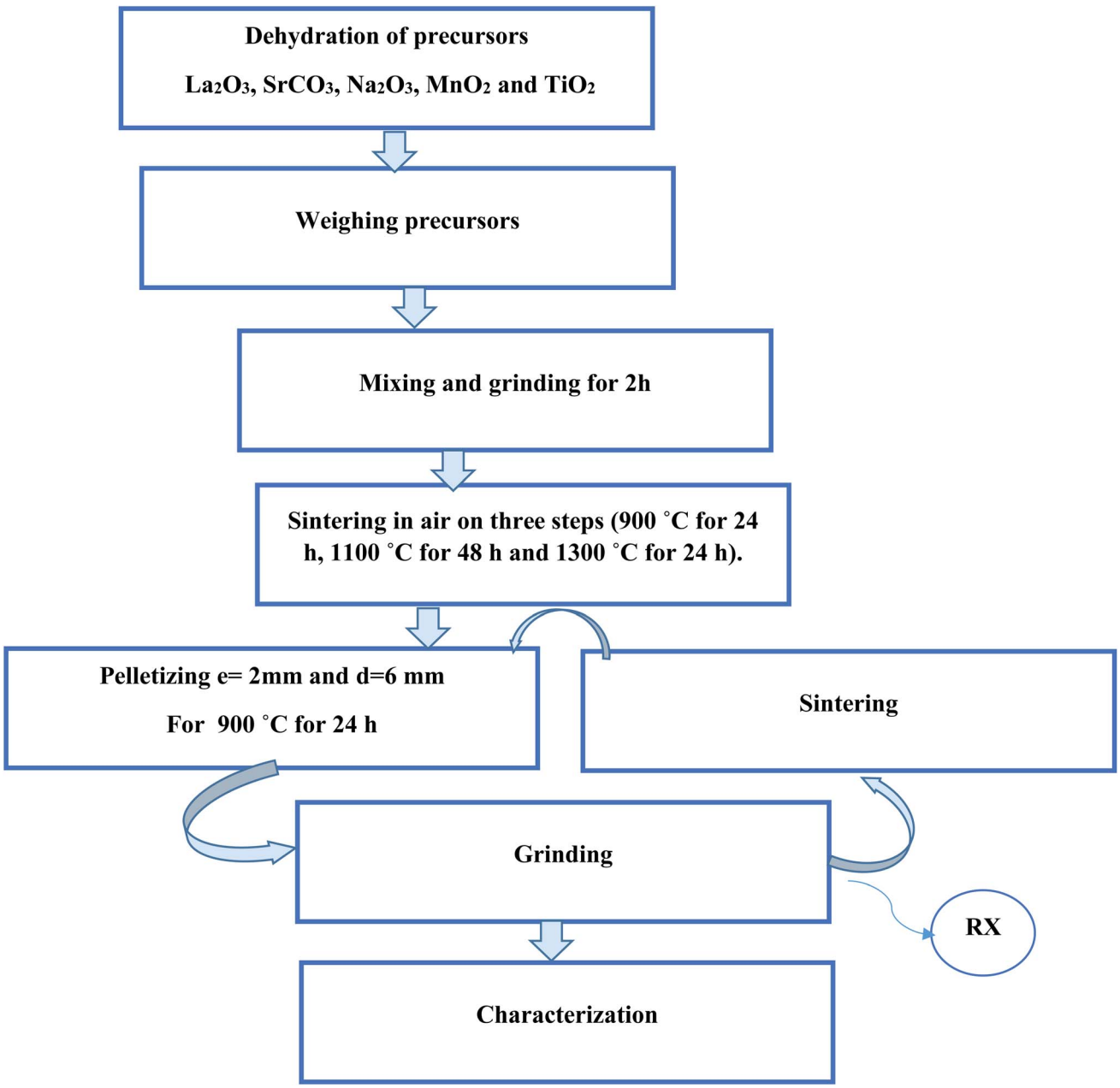

Fig. 1 Flow-chart of LSNMT prepared by a solid-state method.

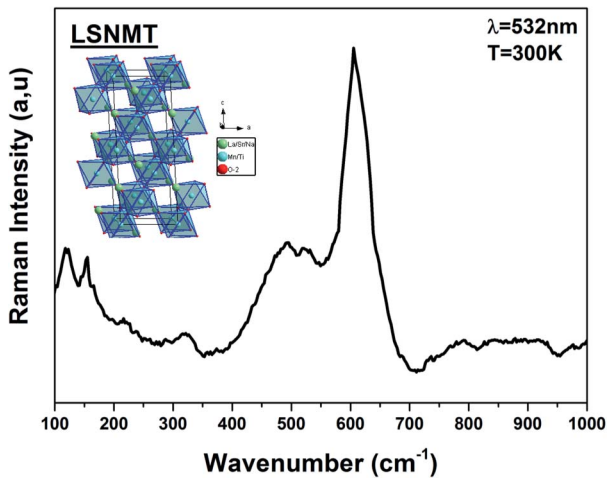

Fig. 2 Raman spectrum of the LSNMT ceramic at room temperature for excitation 532 nm. Inset the crystal structure and the TiO_6 octahedron for our compound.

monochromator and detected by a thermoelectrically-cooled Si photodetector.

4. Results and discussion

4.1. Raman scattering

Recently, several papers argued that optical properties in manganite depend on the Mn–O bond length and the symmetry of MnO_6 confirming the correlation of optical phonon mode with the degree of activation of the Jahn–Teller distortion modes.[23] Usually, Jahn–Teller effects have a major role in the rhombohedral structure manganite related to six equal Mn–O bond lengths governing the dynamic and non-coherent deformation of the MnO_6. Nevertheless, it is well known for this distorted structure that just five Raman-active modes can be detected linked to vibration and stretching oxygen vibrations of the MnO_6.[24,25] For more clarification on the importance of the structural properties and their effect in the optical results, the ABO_3 type perovskite structure with (La/Sr/Na) and (Mn/Ti) cations at A-site and B-site, respectively, is illustrated using "Diamond" program (inset Fig. 2).

After dividing by the factor $n(\omega) + 1$, the Raman spectrum of rhombohedral LSNMT manganite in the frequency [80–1000 cm^{-1}] is illustrated in Fig. 2. The obtained Raman spectrum of LSNMT ceramic exhibits similar behavior in position and profile to that of the data from $LaMnO_3$, which is characteristic by the rhombohedral phase ($R\bar{3}c$).[26–28] In our case, we observed two peaks in the intervals of 100–300 cm^{-1} and 400–700 cm^{-1} associated with phonons of the rhombohedral phase and can be centered at five Raman modes 117, 156, 493, 518 and 605 cm^{-1}. The band at lower frequencies occurs around 117 cm^{-1} from designing the hardening of A_{1g} phonon mode related to the dominant A-site cations (La/Sr/Na) distortions and the electron–phonon coupling strength.[29,30] Also, the peaks at 156 and 493 cm^{-1} are assigned as E_g symmetry mode identified as an internal mode (bending of the MnO_6 octahedra) and we ascribe the two highest peaks at 605 and 518 cm^{-1} to E_g bands defined by the vibration of oxygen in MnO_6 octahedra.[31,32] The proposed assignments and other observed mode wavenumbers are summarized in Table 1, which compares the patterns observed in this study with those recorded according to the several previous research works such as $La_{0.67}Ba_{0.25}Ca_{0.08}Mn_{(1-x)}Ti_xO_3$ by M. Bourguiba *et al.*[33] and $La_{0.65}Eu_{0.05}Sr_{0.3-x}MnO_3$ by R. Bellouz *et al.*[34]

However, the Raman scattering confirms that the crystal lattice and symmetry distortion affect the Mn^{4+} environment and the optical properties in our compound. The same result was reported for other samples such as $La_{0.67}Ca_{0.33}Mn_{1-x}V_xO_3$.[35,36]

4.2. Absorption spectrum

The UV-Vis-NIR absorption spectrum of LSNMT ceramic at room temperature is displayed in Fig. 3. The attribution of the noted absorption bands has been made based on previous research on tetravalent manganese ion (Mn^{4+}) doped perovskite ceramics.[37] The absorption band from 200 nm to 400 nm is related to the charge-transfer (CT) transition from Mn^{4+} to O^2 while three strong absorption peaks in the band from 400 to 700 nm are the contributions of $^4A_{2g} \rightarrow {}^2T_{2g}$, $^4A_{2g} \rightarrow {}^4T_{1g}$, and $^4A_{2g} \rightarrow {}^4T_{2g}$ spin-allowed d–d transitions, respectively, of Mn^{4+} ions.[38] Also, we can see an intense asymmetric wide far-red band referred to a significant overlap of six distinct anti-Stokes and

Table 1 The mode vibration of the Raman spectra of LSNMT at room temperature

	$La_{0.7}Sr_{0.25}Na_{0.05}Mn_{0.7}Ti_{0.3}O_3$ our compound	$La_{0.67}Ba_{0.25}Ca_{0.08}Mn_{(1-x)}Ti_xO_3$ for $x = 0.00$ (ref. 33)	$La_{0.65}Eu_{0.05}Sr_{0.3-x}MnO_3$ for $x = 0.00$ (ref. 34)
Raman modes	Frequency (cm^{-1})	Frequency (cm^{-1})	Frequency (cm^{-1})
A_{1g}	117	110	—
E_g	156	180	—
A_{1g}	—	—	310
E_g	—	—	369
E_g	493	490	495
E_g	518	—	—
E_g	605	605	650

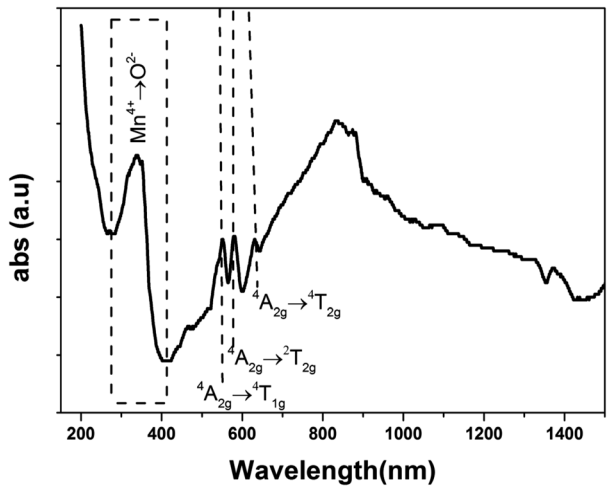

Fig. 3 Absorption spectrum of the LSNMT ceramic in the UV-Vis-NIR region at room temperature.

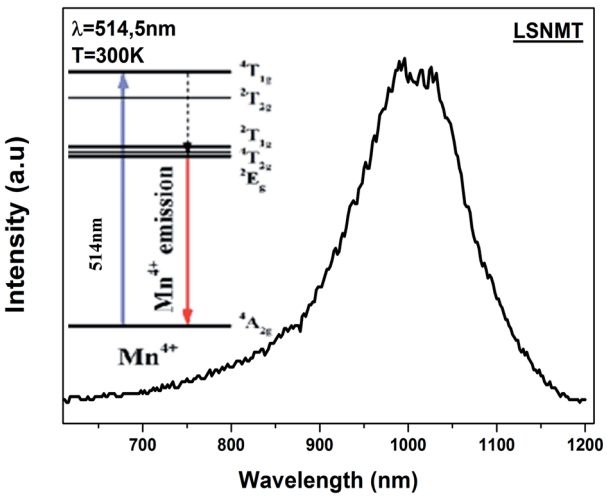

Fig. 5 The emission spectrum of the LSNMT ceramic excited at 514.5 nm at room temperature. Inset schematic energy level scheme of Mn^{4+} ions.

Stokes sidebands between 650 and 900 nm related to the various vibrational modes of $2E_g \rightarrow 4A_{2g}$ transitions in the $[MnO_6]^{8-}$ octahedra for the $3d^3$ electrons.[39] The high absorption efficiency mentioned that Mn^{4+} ion has considerable effects on the comportment of the LSNMT to emit red light.

We studied the light absorption for our compound; in our sample, the absorbance spectrum was procured and presented in Fig. 4. The optical gap of our sample could be estimated by the following equation:[22]

$$(\alpha h\nu)^2 = B(h\nu - E_g) \quad (8)$$

where α, $h\nu$, and B are the absorption coefficient, the energy of the photon, and a constant, respectively.

To compute the energy E_g of the LSNMT sample, we plot $(\alpha h\nu)^2$ *vs.* $(h\nu)$. We obtain $E_g = 4.1$ eV for the $La_{0.7}Sr_{0.25}Na_{0.05}Mn_{0.7}Ti_{0.3}O_3$ compound. This value is similar to that obtained for other perovskites as reported by Kumar *et al.*[39]

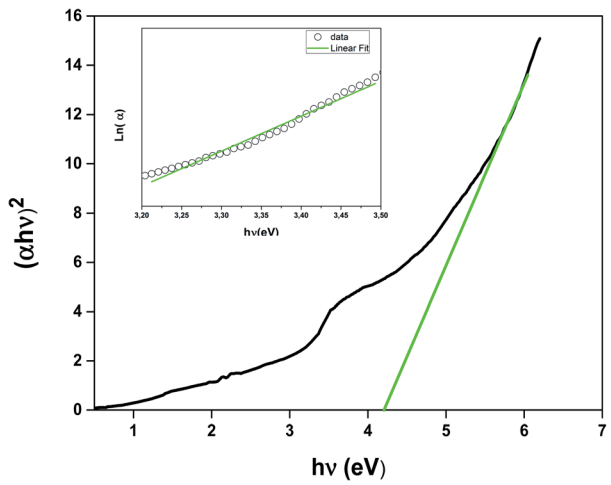

Fig. 4 Energy band gap as a function of the LSNMT ceramic. Inset the plot ln(α) *versus* photon energy ($h\nu$) for LSNMT.

In addition, the electronic bandwidth (W) could be determined by the following equation:[40,41]

$$W \propto \cos[1/2(\pi - (\mathrm{Mn/Ti{-}O{-}Mn/Ti}))]/d_{\mathrm{Mn/Ti{-}O}}{}^{3.5}$$

where (Mn/Ti–O–Mn/Ti) is the bond angle and $d_{Mn/Ti-O}$ is the bond length. We obtain the value $W = 9.23 \times 10^{-2}$ a.u.

In addition, the energy E_g is related to W by the equation; $E_g = \Delta - W$, where Δ is the energy of charge-transfer.[42] The width of defect bands produced in the bandgap is related to E_u.[43] It should be calculated from the formula eq:

$$\alpha = \alpha_0 \exp\left(\frac{h\nu}{E_u}\right) \quad (9)$$

The Urbach energy E_u was measured by tracing ln(α) *vs.* $h\nu$ (inset in Fig. 4). The value Urbach energy E_u obtained in the present work are found to be in low 0.227 eV for the LSNMT ceramic. This suggests the same behavior as reported in other research works, such as on Mn^{4+}-doped glasses.[44,45]

4.3. Photoluminescence properties

The room temperature emission spectrum of the LSNMT ceramic in the Vis-NIR region is illustrated in Fig. 5. Here in our case, we can observe strong emission peaks below 1000 nm. These peaks originate from the charge transfer transition of Mn^{4+}–O^{2-} and spin-allowed transitions of Mn^{4+}: $^4A_{2g} \rightarrow {}^4T_{1g}$, $^4A_{2g} \rightarrow {}^4T_{2g}$ (see in inset Fig. 5), the same behavior as reported previously by X. Gao *et al.*[45]

The working temperature of polycrystalline LSNMT manganite will be lower than the room temperature.

Consequently, thermal stability is particularly important in a manganite. Fig. 6(a) displays the temperature-dependent PL spectrum ($\lambda_{ex} = 514.5$ nm) over the temperature range of 10–300 K for the LSNMT manganite. We notice that the PL intensity decreases with rising temperature due to nonradiative electron transitions increasing with rising temperature.[46,47]

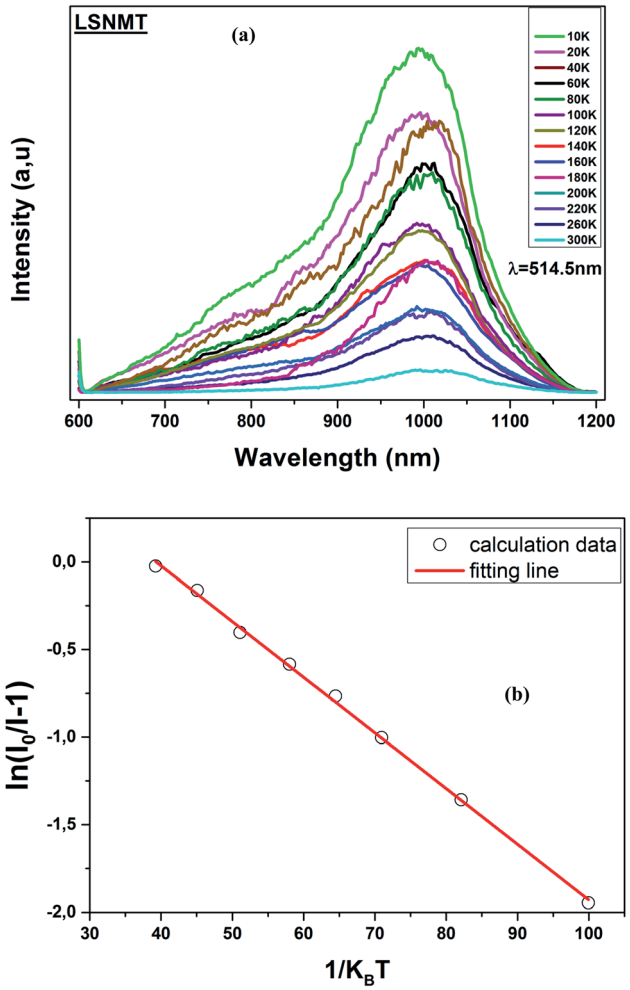

Fig. 6 (a) Temperature-dependent PL emission spectra of the LSNMT ceramic, (b) $\ln[(I_0/I) - 1]$ and $1/k_BT$ for LSNMT.

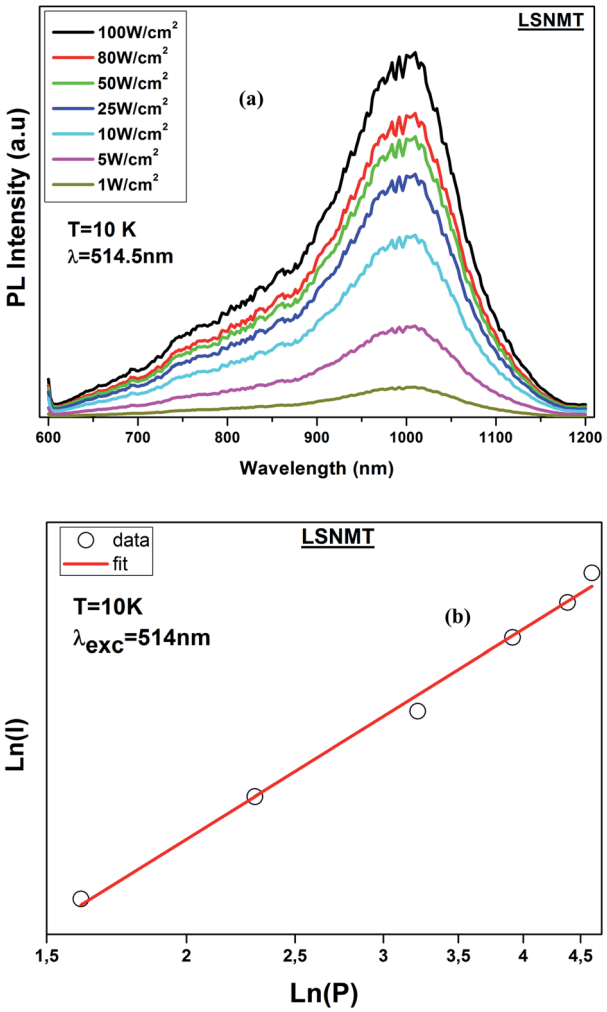

Fig. 7 (a) PL intensity of LSNMT at 10 K at different excitation power densities, (b) log–log plot of PL intensity *versus* excitation power density for ceramic at 10 K.

The activation energy (E_a) was calculated by Arrhenius equation as given in:[48]

$$I(T) = \frac{I_0}{1 + c\exp\left(-\frac{E_a}{k_B T}\right)} \quad (10)$$

This equation can be transformed into the following form:

$$\ln\left(\frac{I_0}{I} - 1\right) = \ln A - \frac{E_a}{k_B T} \quad (11)$$

where I_0 is the PL intensity at the 10 K, A is a constant and k_B is the Boltzmann constant (8.629×10^{-5} eV K^{-1}).

The E_a (0.318 eV) was obtained by plotting $\ln[(I_0/I) - 1]$ and $1/k_BT$ as seen from the plot in Fig. 6(b). This result suggests that LSNMT manganite ceramic present good thermal stability.

In addition, the PL intensities spectra of the LSNMT ceramic using a 514.5 nm laser excitation for the selected excitation power at 10 K, are displayed in Fig. 7(a). It should be noted that the PL intensities rise with an increase of the excitation power and the position of the emission spectra remained constant as the excitation power is raised.

The correlation between PL intensity (I) and the excitation power (P) can be described by the following equation:[48]

$$I \propto (P)^n \quad (12)$$

where n is the number of photons. Fig. 7(b) shown the linear plot of $\ln(I)$ *vs.* $\ln(P)$ as shown in Fig. 7(b) for the band emission for Mn^{4+}. The fitted n values for the band emission are 2, suggesting that a two-photon process has helped to populate the transition in this sample.

The CIE chromaticity of the LSNMT sample at room and at low temperature (10 K) are represented in Fig. 8. The CIE diagram exhibit that the approximate coordinates were related in the red region. The values of CIE coordinates of the LSNMT ceramic are tabulated in Table 2. The resulting CIE chromaticity coordinates of our compound at room and at low temperature (10 K) are (0.6806, 0.3192), (0.6901, 0.3097), respectively.

New technologies based on red phosphor have attracted the attention in industrial applications as white-light-emitting

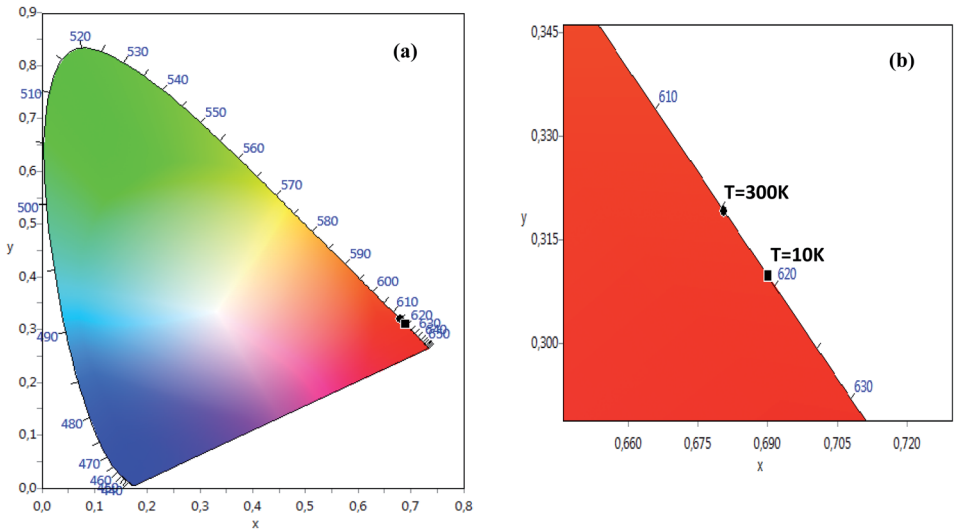

Fig. 8 (a) The CIE chromaticity of the LSNMT sample at room and at low temperature (10 K), (b) the grow of the CIE chromaticity.

Table 2 The values of CIE (*x*, *y*) co-ordinates of LSNMT at room temperature and 10 K

	CIE	
$La_{0.7}Sr_{0.25}Na_{0.05}Mn_{0.7}Ti_{0.3}O_3$	*x*	*y*
At $T = 300$ K	0.6806	0.3192
At $T = 10$ K	0.6901	0.3097

diodes (W-LEDs) to avoid the high color temperature and low color index problem.

Against the high price of this compound, further research and development confirm that transition-metal Mn^{4+}-doped luminescent compounds can be an alternative system to emits red light when excited by near-UV or blue light. However, our investigations of the vibrational and optical behaviors of the LSNMT has demonstrated for the first time that pure red emission persists in our crystal structure. This work can solve the problem of many applications leading to a stable structure of manganite which is correlated to the red pure emission and providing a good candidate for white luminescence display devices.

5. Conclusion

In conclusion, LSNMT ceramics with the polycrystalline perovskite structure have been produced by a solid-state method. The vibrational and optical behaviors were studied. Raman spectrum at room temperature confirmed the rhombohedral phase ($R\bar{3}c$).

In addition, the optical gap and Urbach energy values were determined using the absorption spectrum at room temperature. The PL intensity at room temperature response emits red light (1000 nm). Temperature-dependent PL revealed that our compound has good thermal stability. Using the chromaticity coordinates (CIE), one can see that the LSNMT sample show emission in the red region. All analytical results demonstrate that LSNMT manganite has the potential for considerable applications in white luminescence devices.

Conflicts of interest

There are no conflicts to declare.

Acknowledgements

This research was funded by the Deanship of Scientific Research at Princess Nourah bint Abdulrahman University through a fast-track research funding program.

References

1 J. M. Christ, C. Ngo, T. Batson, C. A. Cadigan, J. Tong, R. M. Richards, R. O'Hayre and S. Pylypenko, Synthesis of high surface area $Ca_xLa_{(1-x)}Al_{(1-x)}Mn_xO_{(3-\delta)}$ perovskite oxides for oxygen reduction electrocatalysis in alkaline media, *Catal. Sci. Technol.*, 2016, **6**, 7744–7751.

2 Q. He, A. Xie, A. Tian and R. Zuo, Superior Energy-Storage Capacitors with Simultaneously Giant Energy Density and Efficiency Using Nanodomain Engineered $BiFeO_3$-$BaTiO_3$-$NaNbO_3$ Lead-Free Bulk Ferroelectrics, *Adv. Energy Mater.*, 2019, **10**, 1903338.

3 J. Han, J. Yin and J. Wu, BNT-based ferroelectric ceramics: electrical properties modification by Ta_2O_5 oxide addition, *J. Am. Ceram. Soc.*, 2020, **103**, 412–422.

4 H. A. Martinez-Rodriguez, K. Onyekachi, A. Concha-Balderrama, G. Herrera-Pérez, J. A. Matutes Aquino, J. F. Jurado, M. H. Bocanegra-Bernal, V.-H. Ramos-Sánchez, J. A. Duarte-Moller and A. Reyes-Rojas, Electronic configuration and magnetic properties of $La_{0.7}Ca_{0.3}Mn_{1-x}Fe_xO_3$ perovskite NPs: the effect of a lower Fe3+ concentration, *J. Alloys Compd.*, 2020, **816**, 152668.

5 A. Abad, A. Cabello, P. Gayán, F. García-Labiano, L. F. de Diego and T. Mendiara, J. Adánez Kinetics of $CaMn_{0.775}Ti_{0.125}Mg_{0.1}O_{2.9-\delta}$ perovskite prepared at industrial scale and its implication on the performance of chemical looping combustion of methane, *J. Chem. Eng.*, 2020, **394**, 124863.

6 Y. Bourlier, B. Bruno, M. Frégnaux, A. Fouchet, D. Aureau and Y. Dumont, Transfer of Epitaxial $SrTiO_3$ Nanothick Layers Using Water-Soluble Sacrificial Perovskite Oxides, *ACS Appl. Mater. Interfaces*, 2020, **7**, 8466–8474.

7 L. Badr, Low temperature conductivity and ion dynamics in silver iodide-silver metaphosphate glasses, *Phys. Chem. Chem. Phys.*, 2017, **19**, 21527–21531.

8 C. Zener, *Phys. Rev.*, 1951, **81**, 440.

9 P. Nisha, S. Savitha Pillai, M. R. Varma and K. G. Suresh, *J. Magn. Magn. Mater.*, 2013, **327**, 189–195.

10 C. B. Larsen, S. Samothrakitis, A. D. Fortes, A. O. Ayaş, M. Akyol, A. Ekicibil and M. Laver, Basal plane ferromagnetism in the rhombohedral manganite $La_{0.85}Ag_{0.15}MnO_{3+\delta}$, *J. Magn. Magn. Mater.*, 2020, **498**, 166192.

11 S. Vadnala, N. B. Srivastava and S. Asthana, Nature of correlated polaron hopping mechanism in A-site cation disorder Nd0.7−xLaxSr0.3MnO3 (x = 0.0, 0.1, 0.2 and 0.3) manganites, *Appl. Phys. A*, 2020, **126**, 155.

12 M. K. Verma, N. D. Sharma, S. Sharma, N. Choudhary and D. Singh, High magnetoresistance in $La_{0.5}Nd_{0.15}Ca_{0.25}A_{0.1}MnO_3$ (A = Ca, Li, Na, K) CMR manganites: correlation between their magnetic and electrical properties, *Mater. Res.*, 2020, **25**, 110813.

13 R. Thaljaoui and D. Szewczyk, Electrical and thermal properties of $Pr_{0.6}Sr_{0.4-x}Ag_xMnO_3$ (x = 0.05 and 0.1) manganite, *J. Mater. Sci.*, 2020, **55**, 6761–6770.

14 B. Arun, M. Athira, V. R. Akshay, B. Sudakshina, G. R. Mutta and M. Vasundhara, Investigation on the structural, magnetic and magnetocaloric properties of nanocrystalline Pr-deficient $Pr_{1-x}Sr_xMnO_{3-\delta}$ manganites, *J. Magn. Magn. Mater.*, 2018, **448**, 322–331.

15 N. Abdelmoula, E. Dhahri, N. Fourati and L. Reversat, *J. Alloys Compd.*, 2004, **365**, 25–30.

16 S. E. L. Kossi, J. Dhahri and E. K. Hlil, Structural, magnetic and theoretical investigations on the magnetocaloric properties of $La_{0.7}Sr_{0.25}K_{0.05}MnO_3$ perovskite, *RSC Adv.*, 2016, **6**, 63497–63507.

17 S. Liu, B. Guillet, C. Adamo, V. M. Nascimento, S. Lebargy, G. Brasse, F. Lemarié, J. El Fallah, D. G. Schlom and L. Méchin, Free-standing La $_{0.7}$Sr $_{0.3}MnO_3$ suspended micro-bridges on buffered silicon substrates showing undegraded low frequency noise properties, *J. Micromech. Microeng*, 2009, **29**, 65008.

18 Z. Lu, X. Zhang, M. Huang, L. Wen, H. Wang, T. Huang and L. Zhou, Characterization and properties of red-emitting Sr_2YNbO_6: Mn^{4+} phosphor for white-light-emitting diodes, *J. Mater. Sci.: Mater. Electron.*, 2018, **29**, 17931–17938.

19 A. Arabi, M. H. Ehsani and M. Fazli, Hydrothermal synthesis of $La_{0.7}Sr_{0.3}MnO_3$ and its application in visible light photocatalytic activity, *J. Mater. Sci.: Mater. Electron.*, 2019, **30**, 19001.

20 P. T. Phong, N. V. Dang, L. V. Bau, N. M. An and I.-J. Lee, Landau mean-field analysis and estimation of the spontaneous magnetization from magnetic entropy change in $La_{0.7}Sr_{0.3}MnO_3$ and $La_{0.7}Sr_{0.3}Mn_{0.95}Ti_{0.05}O_3$, J. Alloy, *Compd*, 2017, **698**, 451–459.

21 T. H. Kauffmann, N. Kokanyan and M. D. Fontana, Use of Stokes and anti-Stokes Raman scattering for new applications, *J. Raman Spectrosc.*, 2019, **50**, 418–424.

22 J. Tauc, *Optical Properties of Solids*, ed. F. Abeles, North Holland, Amsterdam, 1970, vol. 22, p. 903.

23 V. Dediu, C. Ferdeghini, F. C. Matacotta, P. Nozar and G. Ruani, Jahn-Teller Dynamics in Charge-Ordered Manganites from Raman Spectroscopy, *Phys. Rev. Lett.*, 2000, **84**, 4489.

24 L. M. Carrón, A. de Andrés, M. J. Martínez-Lope, M. T. Casais and J. A. Alonso, Raman phonons as a probe of disorder, fluctuations, and local structure in doped and undoped orthorhombic and rhombohedral manganites, *Phys. Rev. B*, 2002, **66**, 174303.

25 X. Kong, J. Wang, Z. Zou, F. Long and Y. Wu, Effect of Sodium Doping on Magnetic and Magnetocaloric Properties of La0.65Sr0.35MnO3 Manganites, *J. Supercond. Novel Magn.*, 2018, **31**, 373–379.

26 S. Keshri Shaw, L. Joshi and S. K. Rout, Influence of BTO phase on structural, magnetic and electrical properties of LCMO, *J. Alloys Compd.*, 2009, **485**, 501–506.

27 V. S. Kolat, H. Gencer, M. Gunes and S. Atalay, Effect of B-doping on the structural, magnetotransport and magnetocaloric properties of La0.67Ca0.33MnO3 compounds, *Mater. Sci. Eng., B*, 2007, **140**, 212–217.

28 I. Fedorov, J. Lorenzana, P. Dore, G. De Marzi, P. Maselli and P. Calvani, Infrared-active phonons of LaMnO3 and CaMnO3, *Phys. Rev. B*, 1999, **60**, 11875.

29 K. Daoudi, H. Alawadhi, S. El Helali, M. Boudard, Z. Othmen, M. Gaidi, M. Oueslati and T. Tsuchiya, Effects of Mn3O4 precipitates on the vibrational properties of epitaxial Ca-doped LaMnO3 films, *J. Phys. D: Appl. Phys.*, 2017, **50**, 395305.

30 I. Krad, O. Bidault, N. Geoffroy and M. E. L. Maaoui, Preparation and characterization of K0.5Bi0.5TiO3 particles synthesized by a stirring hydrothermal method, *Ceram. Int.*, 2016, **42**, 3751–3756.

31 A. E. Pantoja, H. J. Trodahl, A. Fainstein, R. G. Pregliasco, R. G. Buckely, G. Balakrishnan, M. R. Lees and D. Mck. Paul, O(Mn) vibrational bands in dounle-layered manganites: first and second order Raman scattering, *Phys. Rev. B*, 2001, **63**, 132406.

32 J. E. Medvedeva, V. I. Anisimov, O. N. Mryasov and A. J. Freeman, The role of coulomb in magnetic and transport properties of doped manganites: La0.5Sr0.5MnO3 and LaSr2Mn2O7, *J. Phys. Condens. Matter*, 2002, **14**, 4533–4542.

33 M. Bourguiba, Z. Raddaoui, M. Chafraa and J. Dhahri, The investigation of structural and vibrational properties and optical behavior of Ti-doped La0.67Ba0.25 Ca0.08 Mn(1-x)

TixO3 (x =0.00, 0.05 and 0.10) manganites, *RSC Adv.*, 2019, **9**, 42252–42261.

34 R. Bellouz, M. Oumezzine, A. Dinia, G. Schmerber, El-K. Hlil and M. Oumezzine, Effect of strontium deficiency on the structural, magnetic and magnetocaloric properties of La0.65Eu0.05Sr0.3−xMnO3 ($0 \leq x \leq 0.15$) perovskites, *RSC Adv.*, 2015, **5**, 64557–64565.

35 W. L. Zhu, Y. Q. Ma, M. Z. Wu, H. Li, S. Cao, W. J. Yin, K. Yang, G. H. Zheng and Z. Q. Sun, Photoluminescence properties of V-doped La0.67Ca0.33Mn1−xVxO3, *Mater. Res. Bull.*, 2009, **44**, 1867–1870.

36 M. Czaja, R. Lisiecki, A. Chrobak, R. Sitko and Z. Mazurak, The absorption- and luminescence spectra of Mn3+ in beryl and vesuvianite, *Phys. Chem. Miner.*, 2018, **45**, 475–488.

37 Z. Lu, X. Zhang, M. Huang, L. Wen, H. Wang, T. Huang and L. Zhou, Characterization and properties of red-emitting Sr2YNbO6:Mn4+ phosphor for white-light-emitting diodes, *J. Mater. Sci.: Mater. Electron.*, 2018, **29**, 17931–17938.

38 Z. Zhou, J. Zheng, R. Shi, N. Zhang, J. Chen, R. Zhang, H. Suo, E. M. Goldys and C. Guo, *Ab Initio* Site Occupancy and Far-Red Emission of Mn4+ in Cubic-Phase La(MgTi)1/2O3 for Plant Cultivation, *ACS Appl. Mater. Interfaces*, 2017, **9**, 6177–6185.

39 S. Kumar, G. D. Dwivedi, S. Kumar, R. B. Mathur, U. Saxena, A. K. Ghosh, A. G. Joshi, H. D. Yang and S. Chatterjee, Structural, transport and optical properties of(La0.6Pr0.4)0.65Ca0.35MnO3 nanocrystals: a wideband-gap magnetic semiconductor, *Dalton Trans.*, 2015, **44**, 3109–3117.

40 P. G. Radaelli, G. Iannone, M. Marezio, H. Y. Hwang, S. W. Cheong, J. D. Jorgensen and D. N. Argyriou, Structural effects on the magnetic and transport properties of perovskite A1-xA′xMnO3(x=0.25,0.30), *Phys. Rev. B*, 1997, **56**, 8265.

41 M. Medarde, J. Mesot, P. Lacorre, S. Rosenkranz, P. Fischer and K. Gobrecht, High-pressure neutron-diffraction study of the metallization process in PrNi O3, *Phys. Rev. B*, 1995, **52**, 9248.

42 F. Urbach, the Long-Wavelength Edge of Photographic Sensitivity and of the Electronic Absorption of Solids, *Phys. Rev.*, 1953, **92**, 1324.

43 K. Li, H. Lian and R. Van Deun, Site occupancy and photoluminescence properties of a novel deep-redemitting phosphor NaMgGdTeO6:Mn4+ with perovskite structure for w-LEDs, *J. Lumin.*, 2018, **198**, 155–162.

44 C. R. Kesavulu, H. J. Kim, S. W. Lee, J. Kaewkhao, N. Wantana, E. Kaewnuam, S. Kothan and S. Kaewjaeng, Spectroscopic investigations of Nd3+ doped gadolinium calcium silica borate glasses for the NIR emission at 1059 nm, *J. Alloys Compd.*, 2017, **695**, 590–598.

45 X. Gao, W. Xia, T. Chen, X. Yang, X. Jin and S. Xiao, Conversion of broadband UV-visible light to near infrared emission by Ca14Zn6Al10O35: Mn4+, Nd3+/Yb3+, *RSC Adv.*, 2016, **6**, 7544–7552.

46 J. Rihani, V. Sallet, N. Yahyaoui, J. C. Harmand, M. Oueslati and R. Chtourou, Interdot carrier's transfer *via* tunnelling pathway studied from Photoluminescence spectroscopy, *J. Lumin.*, 2009, **129**, 251–255.

47 Z. W. Zhou, J. M. Zheng, R. Shi, N. M. Zhang, J. Y. Chen, R. Y. Zhang, H. Suo, E. M. Goldys and C. F. Guo, Ab Initio Site Occupancy and Far-Red Emission of Mn4+ in Cubic-Phase La(MgTi)1/2O3 for Plant Cultivation, *ACS Appl. Mater. Interfaces*, 2017, **9**, 6177–6185.

48 Z. Raddaoui, B. Smiri, A. Maaoui, J. Dhahri, R. M'ghaieth, N. Abdelmoula and K. Khirouni, Correlation of crystal structure and optical properties of Ba0.97Nd0.0267Ti(1-x)WxO3 perovskite, *RSC Adv.*, 2018, **8**, 27870.